University of California
Santa Barbara

In-Situ Noise Thermometry for Graphene Capacitance Measurements

A thesis submitted in partial satisfaction
of the requirements for the degree

Bachelor of Science
in
Physics

by

Joey Incandela

June 2019

The Dissertation of Joey Incandela is approved.

Professor Andrea F. Young, Supervisor

Acknowledgements

I thank my thesis advisor Prof Andrea F. Young, and graduate student mentor Alexander A. Zibrov for their guidance and support over the last few years. I have learned many crucial skills that will serve me well as I pursue my future in academia. I would also like to thank Mitali Banerjee and Francois Parmentier for their insight into cryogenic amplifier design, and for the example circuits that they provided. Finally I would like to thank Alex Potts, Fangyuan Yang and Liam Cohen for their help in troubleshooting the various analog circuit issues that plagued this project, as well as Rex Bai for the laborious winding of two NbTi inductors.

Abstract

In-Situ Noise Thermometry for Graphene Capacitance Measurements

by

Joey Incandela

This thesis documents the development and testing of a secondary Johnson Noise Thermometry (JNT) system to be used in an eventual search for Anyonic quasi-particles exhibiting Non-Abelian statistics. A descriptive overview of physics relevant to the project is given, followed by a description of the proposed measurement. I then give a schematic overview of the experiment, followed by an explicit description of a custom cryogenic amplifier design that is central to the setup. Following this is a detailed measurement characterizing the performance of the cryogenic amplifier. Finally I discuss a confusing observation about the measurement system's performance during testing, that has delayed completion of the project. I characterize the problem, then present some testable explanations and corresponding solutions that should help resolve it.

Contents

Section 1

Introduction

The Young laboratory is intent on probing the properties of quantum materials in an effort to observe rare electronic states, where characterizations of crystalline heterostructures built around graphene have been of particular interest. Research in the lab is typically organized into three subcategories; First, by making direct transport measurements of graphene heterostructures this lab has probed the physics of 2D electron gases (2DEG) and explored such phenomena as high temperature superconductivity in twisted bilayer graphene, as well as other general phenomena associated with topological order. The group has similarly probed the Integer and Fractional Quantum Hall regimes and made observations of charge carriers with a fraction of the elementary charge, such as quasi-particles with $e/2$ and $e/4$. Secondly, the lab is responsible for developing mechanisms capable of nano-scale imaging of the thermal and magnetic structure of materials. Such measurements rely on a lead evaporation technique that produces nano-scale Superconducting QUantum Interference Devices (SQUIDs) at the tip of small quartz pipettes. Finally, the lab has been working with the methods of Terahertz Spectroscopy to characterize the non-equilibrium transport properties of graphene. This is done using a high intensity pulsed laser source, with which one can make measurements of such properties

as the photo-conductivity, and high-field conductivity of 2D materials on the picosecond scale [1].

However since 2017 [2], the lab has become invested in the search for quasi-particles exhibiting Non-Abelian statistics. In the field of Condensed Matter physics, these particles have been of particular interest due to applications in the development of quantum computers [3]. As proposed in the theoretical work of Moore and Read [4], even denominator states of the Fractional Quantum Hall (FQH) regime such as the $v = 5/2$ state are a promising potential host for experimentally realizable states exhibiting such statistics. In order to probe FQH states for the signature of a Non-Abelian Anyon (NAA), a measurement scheme has been designed around recommendations from the theoretical work of Cooper et al. [5]. From this paper it is apparent that the presence of NAA should be indicated by an entropy signature, visible near the zero temperature limit within an even denominator FQH state.

The group's attempt to gather evidence of NAA quasi-particles will thus hinge on a precise measurement of these two parameters, entropy and temperature, where my work on this project has been primarily concerned with developing a new thermometry system to help us determine temperature. With this perspective, the object of my thesis will be to give a general overview of the physics and design of the measurement as a whole, as well as to report the status of that thermometry system and the function of it's constituent components. The rest of this paper is divided into three sections; In Section 2, I give insight into the physics of NAA as well as the physics of the two relevant parameters that constrain our experimental design. In Section 3, I describe this experimental design in detail with subsections outlining noteworthy components and their functionality. In Section 4 I present a characterization of our custom cryogenic amplifier design, followed by a discussion of a confusing non-linear relationship between the noise spectral density that is reported by the measurement system, and the corresponding source resistor.

Section 2

Background Material

The search for evidence of quasiparticles exhibiting Non-Abelian statistics is synonymous with the search for particles known as Majorana Fermions, predicted by the Italian theorist Ettore Majorana[6] through his analysis of the Dirac Equation. These particles would be charge neutral, and have the property of being their own anti-particle despite also being fermionic in nature.

2.1 Majorana Fermions

In this section I give a brief overview of the thinking that predicts the existence of Majorana Fermions. We start from quantum field theory, with the Lagrangian of the free Dirac field;

$$\mathcal{L} = \overline{\psi}(i\gamma^{\mu}\partial_{\mu} - m)\psi \quad [7] \tag{2.1}$$

Here ψ is the Dirac field, and $\overline{\psi} := \psi^{\dagger}\gamma^{0}$. Note that by varying the action of this Lagrangian w.r.t. $\overline{\psi}$ we can return the relativistic analog to the Schrodinger equation,

the Dirac equation;

$$(i\gamma^{\mu}\partial_{\mu} - m)\psi = 0 \quad [7] \tag{2.2}$$

where ψ would be the four component spinor. This equation can be used to formulate a relativistic description of spin-1/2 particles. Looking back at the Lagrangian, the Gamma matrices γ^{ν} are constrained in that they must obey Clifford algebra, with anti-commutator;

$$\{\gamma^{\nu}, \gamma^{\delta}\} = \gamma^{\delta}\gamma^{\nu} + \gamma^{\nu}\gamma^{\delta} = 2\eta^{\delta\nu} \quad [7] \tag{2.3}$$

As Dirac searched for allowed γ^{ν}, he uncovered solutions with complex elements, which in turn constrained the field ψ to be complex. From this observation, one can derive creation and annihilation operators $a_P^{s\dagger}$, $b_P^{s\dagger}$ from the Dirac field ψ and it's complex conjugate $\overline{\psi}$ that correspond to the creation of a fermion and anti-fermion respectively. In Dirac's formulation the particle and it's corresponding anti-particle share the same mass and charge magnitude but have an opposite sign, which distinguishes the fermion and anti-fermion. When such a fermion/anti-fermion pair collide, as with the electron and positron, they annihilate and produce neutral photons which ensure conservation of charge.

However we made a claim at the beginning of this section that there exists a fermion, indistinguishable from it's anti-matter counterpart, that is also charge neutral. This assertion seems to be in conflict with what we have seen so far from Dirac's formulation. To address this, I would first point out that the annihilation of particles with neutral charge is allowed. Take the example of the neutron. In reality the neutron is made up of

fundamental particles, one up quark and two down;

$$n \rightarrow u + d + d \tag{2.4}$$

The up quark has a fractional charge of 2/3 while the two down quarks have charge -1/3 resulting in a neutral charge neutron. The anti-neutron is similarly constructed from an anti-up quark and anti-down quarks;

$$\tilde{n} \rightarrow \tilde{u} + \tilde{d} + \tilde{d} \tag{2.5}$$

with analogous charges $\tilde{u} \sim -2/3$ and $\tilde{d} \sim 1/3$ [7]. Annihilation of a neutron/anti-neutron pair is thus just the annihilation of the constituent particles, which leads to the same creation of photons as before with conservation of net charge. We now ask how a fermion can be indistiguishable from it's own anti-particle. We know that bosonic particles like the photon are their own anti-particles, as in QFT they are described by a real field ψ such that their creation and annihilation operators are the same. This would be true of fermions if a corresponding real field could be constructed. However Dirac's description of fermions assumed complex γ^ν matrices to be the only possibility, which would imply the Dirac field is also inherently complex. It was Majorana's realization that purely imaginary solutions for the Gamma matrices exist, which allow for this real field describing fermions. This is codified in the Majorana equation;

$$(i\tilde{\gamma}^\mu \partial_\mu - m)\tilde{\psi} = 0 \quad [7] \tag{2.6}$$

which is simply the Dirac equation for imaginary $\tilde{\gamma}^\mu$ and real wave function $\tilde{\psi}$. The class of particles that are permitted by this equation are spin-1/2, charge neutral, indistinguishable from their anti-particle partners, and their fields are invariant to charge

conjugation [7]. We call such particles Majorana fermions.

2.2 Experimental Signature of Non-Abelian Anyons

We can now ask how the field of Condensed Matter physics would hope to make an observation of a Non-Abelian Anyon. As it happens a good place to start is to look at systems hosting paired states of interacting composite fermions [2]. Such states are known to emerge at even denominator filling factors within systems exhibiting the Fractional Quantum Hall Effect (FQHE), and furthermore they are predicted to have an experimentally observable entropy signature.

Before we get into the nature of this entropy signature, let me first give a description of the conditions that give rise to the FQHE; We start with a low disorder 2D system geometry that is host to a 2D electron gas (2DEG). We then take the system to extremely low temperatures and add a strong magnetic field that is out of the plane of the system. In the limit that the field is so strong it dominates the other energies in the system, in particular the Coulomb interactions between electrons, then we can expect electrons in the system to occupy quantized cyclotron orbits corresponding to discrete energy levels, known as Landau Levels [4]. Under these conditions a gap appears in the spectrum of excitations that renders the 2DEG system incompressible, and one can observe Quantized Hall Conductance according to;

$$\sigma_{xy} = \nu \frac{e^2}{h} \quad , \quad \sigma_{xx} = 0 \quad [4] \tag{2.7}$$

Where σ_{xx} is the longitudinal conductivity and ν is a rational number determined by the charge density η and magnetic length l_B;

$$\nu = 2\pi l_B^2 \eta \quad , \quad l_B = \sqrt{\hbar/(eB)} \quad [2] \tag{2.8}$$

Note that one can determine the analogous resistance elements by taking σ^{-1}, therefore $R_{xy} = \frac{1}{\sigma_{xy}}$ and $R_{xx} = 0$. Within this regime, wherever we have half filling of the $N = 1$ Landau Level, we have a chance to observe states that play host to Non-Abelian quasi-particles carrying a fraction $e/4$ of the elementary charge. [4][5][8]. Historically the $\nu = \frac{5}{2}$ state has been a good candidate due to its accessibility through systems such as GaAs heterostructures [8]. However, while there have been observations of the $e/4$ fractional charge [8], such measurements are scarce due to the delicacy of the state, and to this date no definitive measurement confirming the Non-Abelian nature of these fractional charges has been made. Returning to the work of this group, in 2017 the Young lab published findings showing that heterostructures of bi-layer graphene encased in boron nitride are a powerful foundation for probing FQH states, as they have very low disorder and are highly tunable [2]. With a suitable device, we expect to be sensitive to a variety of even denominator states such as $\nu = \pm\frac{1}{2}, \pm\frac{3}{2}...$ as well as the famous $\frac{5}{2}$ state.

As for the detection of NAA signatures, we look to the theoretical work of Cooper et al. [5]. As they describe, Non-Abelian states have the important property that the ground state is made exponentially degenerate by the number of quasi-particles in the system. This is because Majorana fermions can be trapped by topological defects in the system, creating bound states called Majorana modes, where the number of ways we can occupy these modes gives rise to the degeneracy. In the example of the $\nu = \frac{5}{2}$ state described by the Moore-Read wavefunction [4], the ground state degeneracy formed goes as $2^{N_{qp}/2-1}$, where N_{qp} is the number of quasiparticles [5]. As a result, occupation of the Majorana modes leads to an entropy contribution;

$$S_{MR} = \frac{1}{2} k_B n_{qp} ln(2) \tag{2.9}$$

(Note the subscript refers to the Moore-Read state.) For quasi-particles of charge $e/4$

we expect;

$$n_{qp} = 4|n - \frac{5n_o}{2}| \tag{2.10}$$

Here n is the electron density by area and $n_o = \frac{eB}{h}$ where B is the applied magnetic field. This entropy should be temperature independent, and thus we expect in the limit as $T \to 0$ this behaviour should dominate and become measurable. Cooper et al. have further reduced this problem by observing that this entropy is indirectly measurable through either the chemical potential μ or the magnetization density m of the system [5]. For our experiment, we have chosen to track down the chemical potential, where we have the general Maxwell relation;

$$\left(\frac{\partial S}{\partial n}\right)_T = -\left(\frac{\partial \mu}{\partial T}\right)_n \tag{2.11}$$

which reduces in the limit of small T and constant perpendicular magnetic field B to;

$$\left|\left(\frac{\partial \mu_{MR}}{\partial T}\right)_{B,n}\right| = k_B 2ln(2) \tag{2.12}$$

where the Non-Abelian contributions to entropy have become dominant. This relation has been shown to be general, and not restricted to the $\nu = \frac{5}{2}$ factor or systems governed by the Moore-Read state [5]. Thus we can hope to probe for Non-Abelian statistics within any of the even denominator states that are available in our sample. The problem of measurement is thus reduced to a precise measurement of μ and T, where if we can show from our measurement that the projected y-axis intercept matches this value $k_B 2ln(2)$, then we will have found strong evidence for the Non-Abelian Anyon. I can now introduce the proposed measurement setup that hopes to capture these two parameters.

Lets start with the measurement of the parameter μ. Figure 2.1 gives a rough description of the graphene heterostructure we hope to use for the measurement. Using a

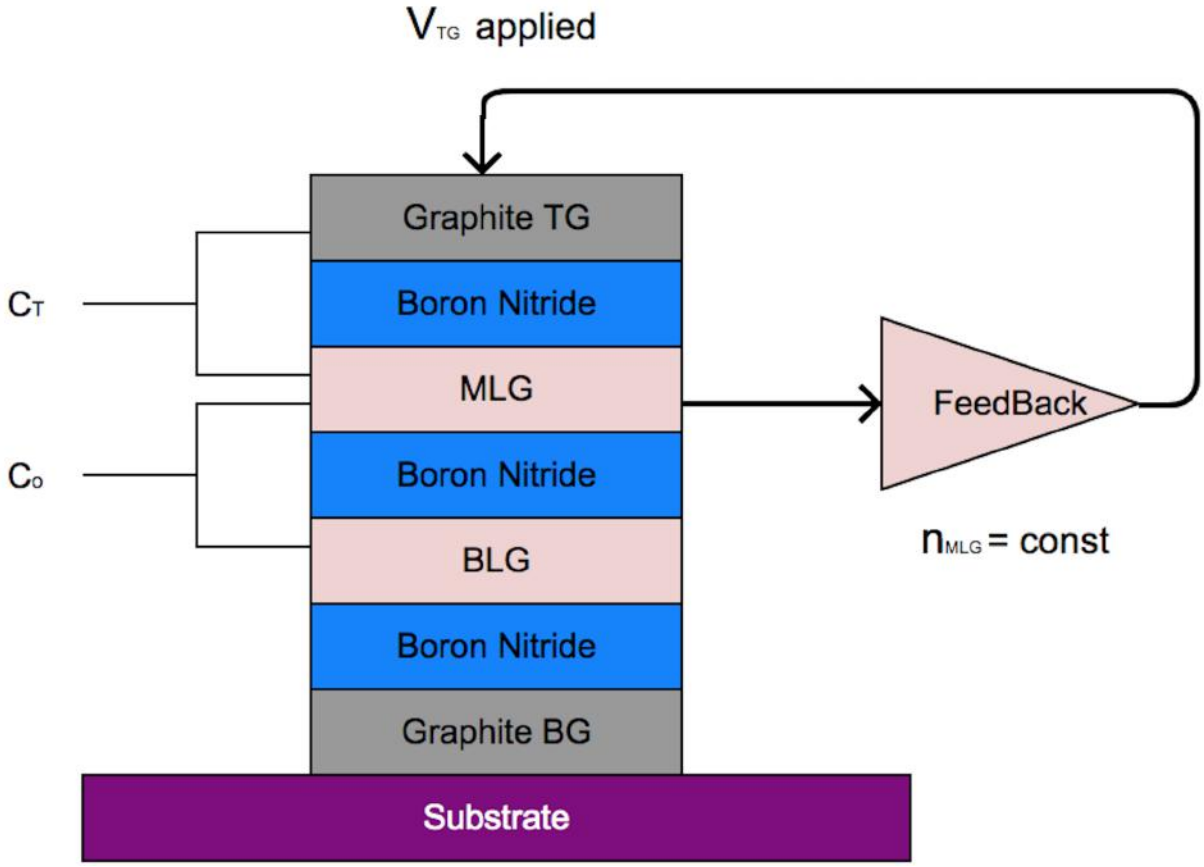

Figure 2.1: Cartoon of the proposed sample geometry. Electrical connections are made to the graphite top and bottom gates (TG,BG) as well as to the mono/bilayer graphene layers (MLG,BLG) for control. A feedback mechanism keeps the carrier density of the MLG layer constant through modulation of the voltage applied to the top gate. The inter-layer capacitances C_T and C_o are taken to be geometric capacitances, and are determined through measurement of the Boron Nitride layers during assembly.

feedback control loop, we fix the carrier density of the monolayer graphene (MLG) by modulating the voltage applied at the graphite top gate V_{TG}. For constant MLG carrier density, we can directly relate the top gate modulation to the chemical potential of the bilayer graphene (BLG) through the capacitances C_T and C_o according to the relation;

$$C_T \Delta V_{TG} = C_o \Delta \mu_{BLG} \tag{2.13}$$

Thus for constant C_T and C_o, a measurement of chemical potential is made by recording the top gate modulations. Two other members of the Young lab group, my graduate student mentor Alexander Zibrov and post-doctorate Fangyuan Yang, are to be credited for the work of fabricating a sample with such a geometry, as well as for the development of the feedback control loop.

The bulk of my work for this project has been in developing a system capable of measuring the parameter T. This is done by making use of the phenomenon of Johnson-Nyquist Noise, wherein a resistor acts as a source of white noise whose magnitude is proportional to the square root of the temperature. This is codified in the formula;

$$V_n^2 = 4 k_B T R \Delta f \quad [9] \tag{2.14}$$

where V_n is the noise signal generated by a resistor R at some temperature T over some frequency bandwidth Δf. By making measurements within the FQH regime we have the advantage of a system with quantized Hall resistance, such that we can extract the parameter R almost exactly. Thus measurements of the noise floor of our graphene sample while we are within the FQH regime should be a direct measurement of the charge carrier temperature. Such a measurement of temperature has the advantage of being non-invasive and in-situ, as a direct measurement of carrier temperature can be made without

losses through whatever degrees of separation nominally exist between the sample and a conventional thermometer. Our Johnson Noise Thermometry (JNT) system is therefore designed to track changes in sample temperature that may otherwise go unseen by the primary thermometry system of the probes used in our dilution refrigerator. This system will be the subject of Section 3.

2.3 Applications to Quantum Computation

The interest in Non-Abelian anyons for the development of quantum computers can be explained with an overview of the properties of the Abelian and Non-Abelian statiscal regimes. In an Abelian statistical regime an exchange of particles can result in a change of phase that is determined by the particle's classification as fermion, boson, or anyon. This exchange of particles does not affect the state of the system or the associated observables. As is widely known, bosons and fermions are respectively symmetric and antisymmetric under exchange, corresponding to a change of phase $|\psi_1\psi_2\rangle = -|\psi_2\psi_1\rangle$ for fermions, and $|\psi_1\psi_2\rangle = |\psi_2\psi_1\rangle$ for bosons [10]. All particles in three dimensional systems are bosonic or fermionic, but in a two dimensional system geometry quasi-particle behaviour may become anyonic in nature. The name anyon is descriptive here, as such quasi-particles can pick up any phase corresponding to some θ such that;

$$|\psi_1\psi_2\rangle = e^{i\theta}|\psi_2\psi_1\rangle \quad , \quad 0 \leq \theta \leq 2\pi \quad [10] \tag{2.15}$$

Such a two dimensional system geometry may seem intangible, but as it happens materials such as graphene and boron-nitride have the propensity to form quasi-2D layers as thin as a single atom, which is enough to manifest the phenomena of 2D physics.

In contrast to Abelian particles, the Non-Abelian statistical regime allows not only for

a change of phase under exchange of two particles, but for a unitary transformation to an orthogonal state [8][3]. Furthermore, the states of a system of Non-Abelian Anyons exist in a protected space $\mathcal{M}_{d1,\ldots,dn}$ that is not affected by local measurements or perturbations unless the constituent particles are brought close together [3]. Thus if Non-Abelian anyons were proven to exist, this could theoretically give us a robust way to encode information into qubits; we simply bring particles together and unlock the protected space $\mathcal{M}$, perform a rotation or unitary operation that we control to encode data in the particles' state, then increase the separation distance to lock the encoded data in $\mathcal{M}$, where it is accessible through local measurement. In this way, one could ideally create a topological quantum computer whose qubits naturally resist decoherence.

Section 3

Design and Development

3.1 Dilution Refridgerator Probe

The main workhorse of this experiment will be a Bluefors cryogen free Dilution Refrigerator (DR) that is responsible for supplying the sample conditions required for the FQHE to manifest (See Figure 3.1). There are five cooling stages, starting with the bulk cooling stage at 50 Kelvin, followed by a series of 4 K, .7 K, and 100 mK stages, with a final base temperature of $\sim$ 10 mK. The first couple of cooling stages are handled by a two stage pulse tube cooling system, which in a typical cryogen free DR provides cooling power at the first stage on the order of $\sim$ 50 Watts, and cooling at the second stage of order $\sim$ 1.5 Watts [11]. By the time we get to the final cooling stage the cooling power can be very small, on the order of μW. Samples are introduced on a custom probe design that is built around a Bluefors standard (Figure 3.1). The probe is cooled at each stage of the DR through thermal conduction between a cooling plate in the DR and a gold plated puck on the probe that is positioned so as to be flush with the plate. For each stage we want to maximize thermal conduction between puck and DR, but we want to minimize the thermal exchange between stages. We thus maximize the area of contact

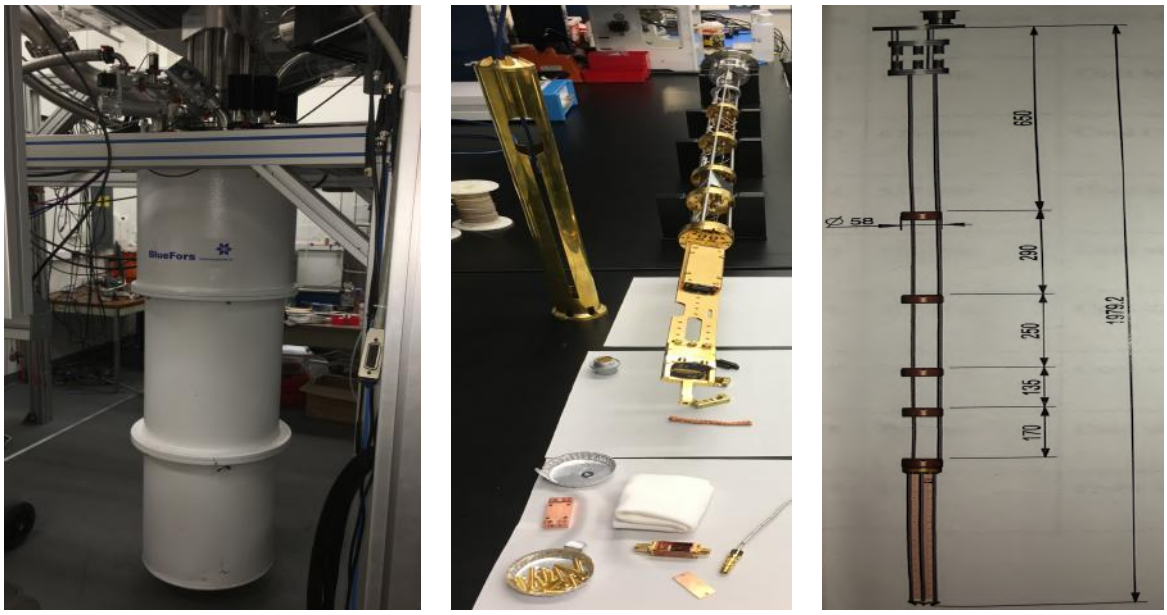

Figure 3.1: Left; the Cryogen free Dilution Refrigerator operating in the Young lab. The system is nominally capable of reaching a base temperature of 10mK, and of providing an axial magnetic field with a maximum strength of 14 Tesla. Center; the custom probe designed and built for use within the DR for this noise thermometry project. Visible in the photo are the five gold plated pucks that make thermal contact with the DR. A brass Faraday cage stands to the left, which is affixed the the final puck of the probe. Right; Schematic of the standard Bluefors probe model, used as the basis for the probe at center. (All dimensions are given in mm)

between the puck and the DR, and use gold plated copper which has good thermal conductivity. During operation the entire interior chamber of the DR is held under vacuum, which thermally isolates each stage except for along the triad of rods that are structurally integral to the probe. To minimize exchange we thus minimize the contact area between stages by making the rods very thin, and we make them out of steel which is a poor thermal conductor.

Protruding from the end of the base temperature puck is a rectangular rod that is also gold plated, and has perforations for attaching two passive components for filtration and electron thermalization. There is also a perpendicular PCB near the tip of the rod that houses our graphene structure (Figure 3.1, middle). This orients our samples so

that the axial magnetic field of the DR will point out of plane.

3.2 Component Description

With this understanding of the greater physical and material structure of our setup, we can now move to a description of the circuit structure that is mounted on the probe. In essence, the probe can be thought of as two separate circuits running in parallel, with one circuit handling the measurement of the Johnson Noise temperature signal, and the other handling the feedback mechanisms that allow for measurement of chemical potential. Figure 3.2 gives a detailed schematic of the two parallel circuits.

From the noise thermometer perspective, the objective of the circuit is to make sure the low temperature Johnson Noise signal sourced from the sample is not drowned out by larger sources as we move it to room temperature where it can be measured on a spectrum analyzer. (I note that the rough structure of the circuit is based on a design used by Iftikhar et al.[12].)

Tracing the path of the signal through Figure 3.2, we start with the quantized hall resistance R_{xy} which generates a white noise spectrum proportional to the filling factor ν. Around the minimum expected base temperature of the DR (10mK) with a factor of say $v = \frac{1}{2}$, the spectral density of the signal from R_{xy} would be on the order of $\sim 170\frac{pV}{\sqrt{Hz}}$. This signal propagates through superconducting coaxial cables with Niobium-Titanium (NbTi) cores at the lower temperature stages. The signal encounters an LC resonator to chassis ground formed by a hand wound NbTi inductor in parallel with the finite cable capacitance ($\sim$ 100pF) of the coaxial line. An inductor is used so as to impedance match this cable capacitance in front of the cryogenic amplifier. We do this to effectively exchange a lossy RC filter formed by the sample resistance and this small capacitance, for a band pass filter that is effectively loss-less at resonance. In the final setup we would

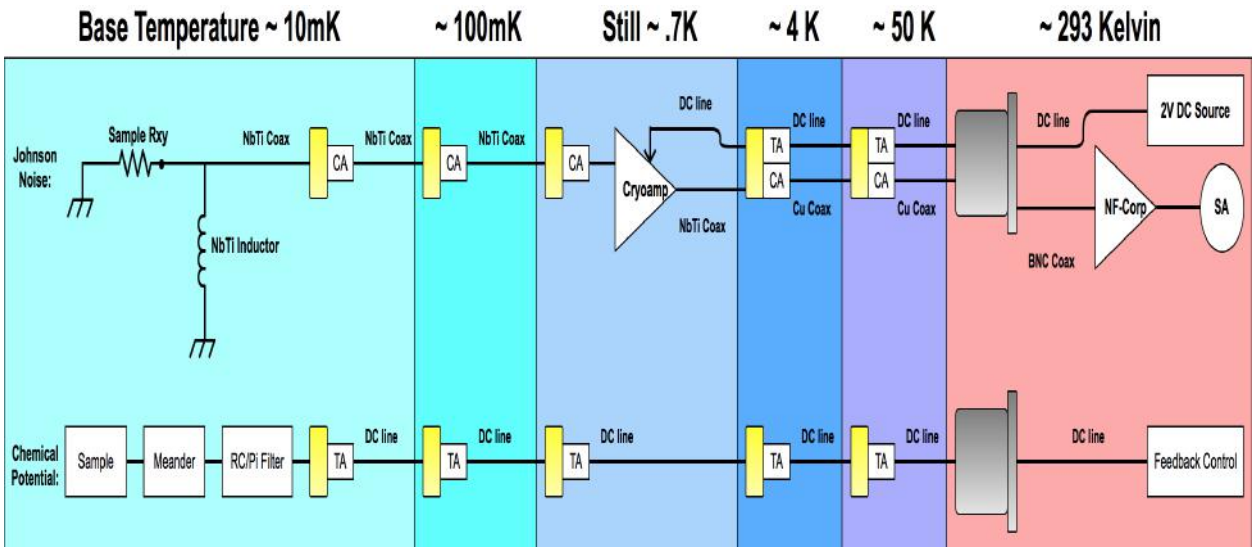

Figure 3.2: Experimental setup from the viewpoint of two distinct circuits. Here 'coax' is shorthand for coaxial cable, where colder stages have Niobium Titanium (NbTi) superconducting coax between stages. At the warmer end, these cables are replaced with non-superconducting copper (Cu) coax, that connect to standard BNC coax outside the Dilution Refrigerator. A spectrum analyzer (SA) interprets the transfered R_{xy} signal. Cryogenic attenuators (CA) are positioned at the cooling stages as recommended in the original Bluefors probe design. These limit the power of incoming signals, so as to not overwhelm the cooling power of the lower stages. Non-Superconducting twisted wire pairs (DC line) supply a DC bias to the cryogenic amplifier, and the same type of wire is used to carry low frequency excitations to the sample in the chemical potential circuit. For each cooling stage traversed, these DC lines are wrapped around and epoxied to a gold plated bobbin so as to thermally anchor (TA) them to that stage.

tune this inductance such that the resonance frequency of the filter aligns with the largest gain region of the cryogenic amplifier.

The signal then meets the first amplification stage. This cryogenic amplifier sitting at 4 Kelvin is characterized in the next section, as it is a custom design that took a few iterations to get right. For now it is just worth noting that this amplifier should give us a linear gain factor of about 8, while drawing only ∼3.7mW of power for a 2 Volt bias. This power drawn is well below the active cooling power of the 4 Kelvin stage of the DR, such that we expect the amplifier will not upset our cryogenic system. After this gain stage we expect our signal to be on the order of $1.4\frac{nV}{\sqrt{Hz}}$. The signal travels the rest of the distance to room temperature through two stages of non-superconducting copper coaxial cable. At room temperature we pass the signal through another amplification stage using an NF-CORP model SA-220F5 low noise FET amplifier. The input noise floor of this amplifier nominally sits at $.5\frac{nV}{\sqrt{Hz}}$ for the frequency range we expect to set our band-pass resonance to, so the noise signal we hope to amplify should sit safely above the floor. Using this device in our expected frequency range, our signal should be amplified by a factor of 46 dB (or 200 in linear units), before it is finally processed by a spectrum analyzer. In our case we have been using a Zurich model MFLI lockin-amplifier with built-in spectrum analyzer functionality. By this point our signal should be well above the noise floor of this measurement device, which is around $2.5\frac{nV}{\sqrt{Hz}}$. Also at room temperature is the DC source used to bias our amplifier. I note that for testing and development so far, an SRS model SIM928 isolated voltage source has been used to provide this bias, which was chosen primarily for it's ultra-low noise DC output. As is reported in it's datasheet, the source is designed to have a noise floor on the order of 10 μV for the 0Hz $\rightarrow$ 1kHz frequency range, after which the noise spectral density drops to just a few $\frac{nV}{\sqrt{Hz}}$. This near DC noise does not disrupt the measurement and can be ignored, as it is far outside the frequency band of our filtered signal.

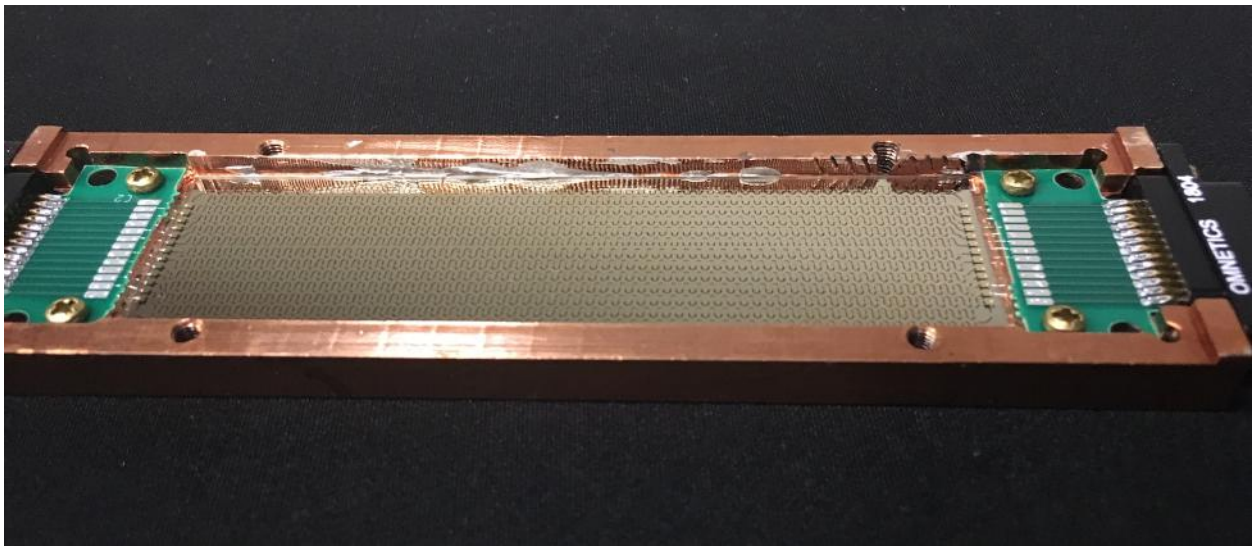

Figure 3.3: The meander component, shown in a gold plated enclosure. Also visible in the picture are the 13 chromium on gold lines patterned onto the quartz substrate.

The circuit diagram on the chemical potential side of the probe is somewhat less complex. Low frequency signals from DC to a few kHz are supplied at room temperature to control the graphene heterostructure at base temperature. For example the feedback control loop operates around 10Hz. A group of 12 non-superconducting twisted wire pairs transport these signals, where we have chosen to use 36 gauge phosphor bronze wires with a heavy polymide insulation.

This group of wires is thermally anchored to each cooling stage using a small gold plated bobbin about three quarters of an inch tall with an inner diameter of .3 inches. Roughly 7 inches of each wire pair is wrapped around this bobbin, and epoxied in place. The epoxy used was the Loctite Stycast 2850FT along with the low viscosity catalyst 23LV. At the base temperature stage, we break out 13 wires (leaving 11 spare) and pass these through two final passive components before reaching the sample. The enclosures for both of these components have a large area of contact with the probe and are also made from gold plated copper to help put them at thermal equilibrium with the rest of the stage. In the first component, a series of RC and π-filters strip noise from the

input signal in the near DC range up to a few MHz. Next a 13 line meander is used to help thermalize the electrons in the system before reaching the sample. The meander is fabricated as follows; we spin a thin layer of resist onto a piece of single crystalline quartz. Using a mask to outline the trace pattern, we then set this pattern onto the quartz surface using UV lithography. A thin film of chromium on the order of ∼10nm is then deposited, followed by ∼ 1000nm of gold, which bond to the quartz in the pattern defined by the resist. Finally the material is annealed in a mixture of Argon and Hydrogen (Ar/H_2) gas, producing the device shown in Figure 3.3.

3.3 RF Cryogenic Amplifier

Requiring special attention, the first amplification stage of the filter probe at ∼4 Kelvin is a custom radio frequency amplifier based on the Broadcomm ATF34143 Pseudomorphic High Electron Mobility Transistor (PHEMT). A word on these transistors; they are now deprecated and are rapidly becoming scarce. Furthermore they are intended for use at room temperature and for frequencies in the GHz range. It is notoriously difficult to find transistors that perform at cryogenic temperatures, and it so happens these are known within the field to remain functional and stable, with reasonable gain in the MHz range. The transistor is thus somewhat of a hereditary component passed on to us by Francois Parmentier, a physicist who has done similar noise thermometry experiments. The first amplifier design we tried to work with was also based on a common emitter amplifier suggested to us by him, and a variant of this has been used in his own work [12]. (It's circuit diagram is shown in Figure 3.4). I therefore note that for future designs research may be required to determine a suitable replacement, preferably a transistor that is still supported and/or in production.

Let me now describe the functionality of this amplifier by again tracing the input

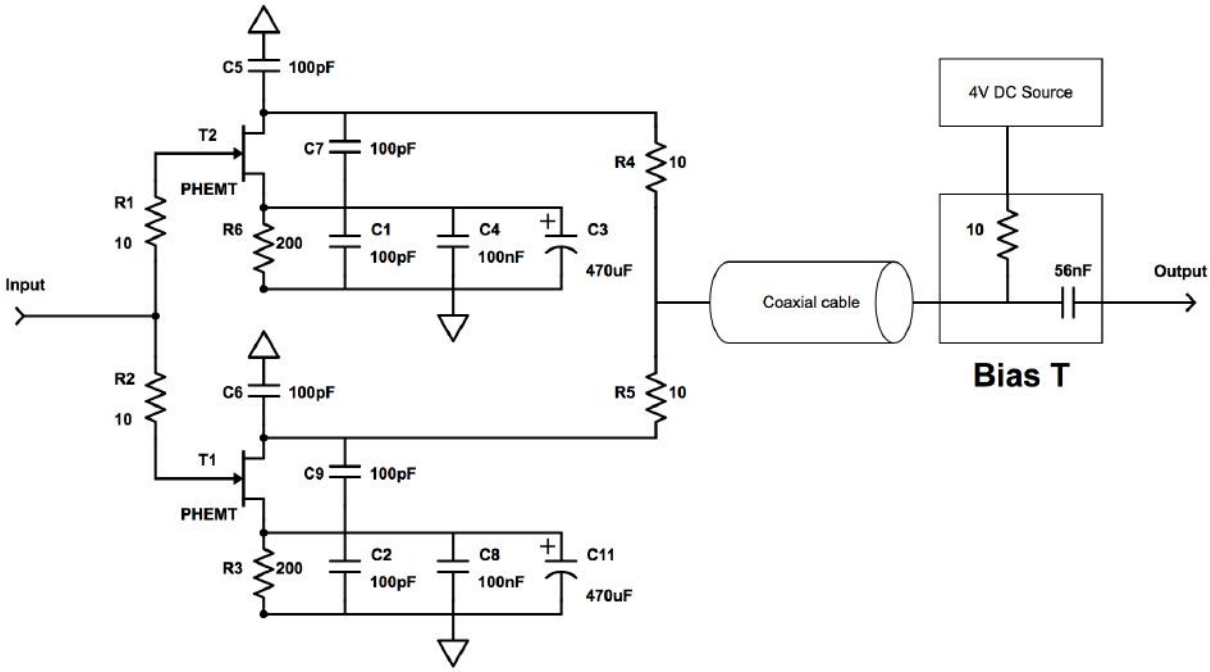

Figure 3.4: Circuit schematic for the common emitter cryogenic amplifier. The device consists of two parallel amplifiers, who are biased at their output through a separate Bias T component. The amplifier bandwidth is set by two factors; the low frequency cutoff is the result of a high pass RC filter at the transistor source, while the high frequency cutoff is set by the transistor's performance in these operating conditions. The stability of the amplifier is controlled through the capacitors C7 and C9 that straddle the transistors.

signal through the circuit, while referring to the schematic in Figure 3.4. We see the input is filtered through a high pass at the transistor source, formed by a 200 ohm resistor and three capacitors. The capacitance values are chosen to be large in this design so as to push the filter's RC roll-off into the range of a few tens of kHz, giving the amplifier a large operating bandwidth. A 100pF capacitor connects each transistor's drain to the source, which helps improve the amplifier's stability and behaviour when it is connected to a high reactance load. The amplifier is structured in such a way that the transistor quiescent bias has to be provided through the same line as the output, which is accomplished using a simple external circuit consisting of a small resistor and a capacitor acting as a DC block. Starting from the DC source, we see that a 4V DC signal encounters the 10 ohm resistor of the Bias T component, followed by the resistor R4 or R5 which connect to the transistor drain. The resistors R6 and R3 tie the transistor source pins to ground, where the ratios of R4/R6 and R5/R3 set the bias points for each transistor. For a 4V bias, the current drawn in this configuration should be $\sim$36mA, corresponding to $\sim$18mA per common emitter amplifier in the circuit. Heading in the opposite direction of the bias, the AC output signal is separated from the DC bias with a 56nF blocking capacitor before being sent on to later stages.

In working with this amplifier design we encountered a variety of issues. First and foremost, finding a compact 470μF capacitor that functions at cryogenic temperatures is difficult. This lead to the erroneous choice of a tantalum based electrolytic capacitor to fill the role of C3 and C11. It turns out these capacitors have two major drawbacks; they are very sensitive to electrostatic discharge (ESD) which makes them difficult to handle, and more importantly they seem to breakdown at cryogenic temperatures. When exposed to one of these two conditions the failure mode of the capacitor is to fail-open, which shorts the 200 ohm resistor that was limiting the bias current at the transistor source, drawing currents up to 200mA if the compliance of the DC source is not set carefully. The

Figure 3.5: Left; Common emitter amplifier, in a copper enclosure. The large orange components that are visible in the photo are the 470μF capacitors that were eventually removed. Right; The more compact Cascode amplifier design that we have chosen to use, suggested by Mitali Banerjee from the Heiblum group. Visible in this photo is a small pin passing through the enclosure on the left. This is the feed-through capacitor used to supply the bias. Heiblum group website: https://heiblum.weizmann.ac.il/

PHEMT transistors do not take kindly to such a large amount of DC power, so failure of one of these capacitors typically lead to the destruction of the associated transistor. This problem was mediated by simply removing the tantalum capacitor, where we sacrificed the very low frequency roll-off but our band pass filter is set at such a frequency that this roll-off wasn't beneficial anyway.

Another issue with this amplifier is it's size (See Figure 3.5 left). It is somewhat difficult to fit the width of this design into the allocated space on the probe. The large footprint of the PCB is primarily due to the fact that we fit two common emitters in parallel [13], which was done to improve the signal to noise ratio. This is known to get better as we add amplifiers in parallel, so we would ideally fit more if the space permitted. For these reasons, we decided to shift to a more compact design suggested to us by Mitali Banerjee, a member of the Moty Heiblum group at the Weizmann Institute of Science. For comparison, the alternate amplifier is featured alongside the old design in Figure 3.5.

The amplifier is a cascode amplifier designed to specifically avoid the cutoff frequency

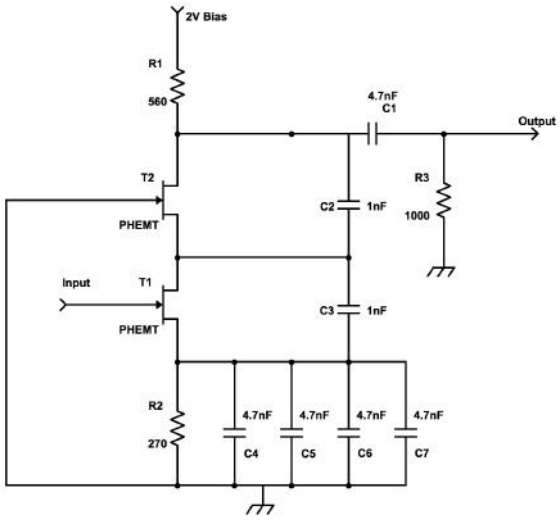

Figure 3.6: Circuit schematic for the Cascode Amplifier design. The amplifier has an inherent bandwidth which is set by two factors; the low frequency cutoff is the result of a high pass RC filter at the source of T1, while the high frequency cutoff is inherent to the transistor operating conditions as with the last design. Another similarity with the last design are the 1nF capacitors C2 and C3 straddling the transistors, which again handle the amplifier stability.

problem caused by the Miller effect, which plagues common-emitter and common-source circuits [13]. In addition to being smaller, this amplifier has the advantage of drawing less power while providing slightly better voltage gain. The amplifier also has no ESD sensitive components and has thus far proved to be robust to casual handling, unlike it's predecessor. To describe the functionality of this amplifier design, let us trace the input signal through the circuit of Figure 3.6 as before. From the input the signal is sent to the gate of the transistor T1, which is in a common emitter configuration. We note that the source of T1 is connected to an RC filter that is very similar to the last design, though in this case small 4.7nF capacitors are set in parallel, resulting in an RC time constant of $\tau = 5.08\mu s$ and/or a low frequency roll-off sitting at $\sim$ 200kHz. Meanwhile the drain of T1 sees the input impedance of transistor T2 acting as a load. The load at the drain sets the voltage gain of T1, where because the gate of T2 is grounded, its input impedance is

very small, effectively killing the voltage gain of T1. This low gain at the input transistor in turn circumvents the effect of the Miller capacitance measured between the gate and drain of T1 [13], and in the end we recuperate the lost voltage gain thanks to T2. Thus from the drain of T2 our wide bandwidth, amplified signal proceeds to the output through a DC blocking capacitor C1. Note this output is referenced to ground through a 1kΩ pull-up resistor. Meanwhile the DC bias is supplied directly to this amplifier without the need of an external Bias T component, passing through the copper enclosure with the help of a feed-through capacitor (i.e. a capacitor to ground in parallel with R1). This component is visible in the right pane of Figure 3.5. We note the operating point of the transistors is set by the ratio of R1 and R2, and in accordance with Mitali Banerjee's recommendations, a bias of 2V is supplied at R1. This bias point was tuned so that the lower transistor T1 is always operating in what is called the pinch off region [13], though this choice is also a reasonable compromise between the amplifier's gain and the power dissipated. For this bias the DC current is typically 1.85mA, which allows us to estimate the power drawn to be ∼3.7mW. This concludes a qualitative description of the measurement setup. In the next section I provide some data on the performance of this component.

Section 4

Measurements of Component Behaviour

4.1 RF-Amplifier Characterization

Our custom cascode cryogenic amplifier was tested independently from the rest of the Bluefors measurement probe components, where a separate probe with a much simpler design was built specifically for testing in liquid nitrogen and liquid helium. The probe is essentially just a steel tube that is 1/2 of an inch in diameter, through which we thread two stainless steel coaxial lines to carry the input and output signals, with one twisted pair of wires to provide the amplifier bias. Fixed to the tube diameter of the probe with a compression fitting, a large flange connects to and seals the top of the dewar, where we typically use a 25 litre nitrogen dewar or a 100 litre helium dewar for testing. For each test the amplifier is placed at the end of the probe, and lowered until it is immersed in liquid. This immersion ensures that the amplifier is held at or below the boiling temperatures of nitrogen or helium during testing. Note the boiling points of nitrogen and helium are 77.36 Kelvin and 4.22 Kelvin respectively.

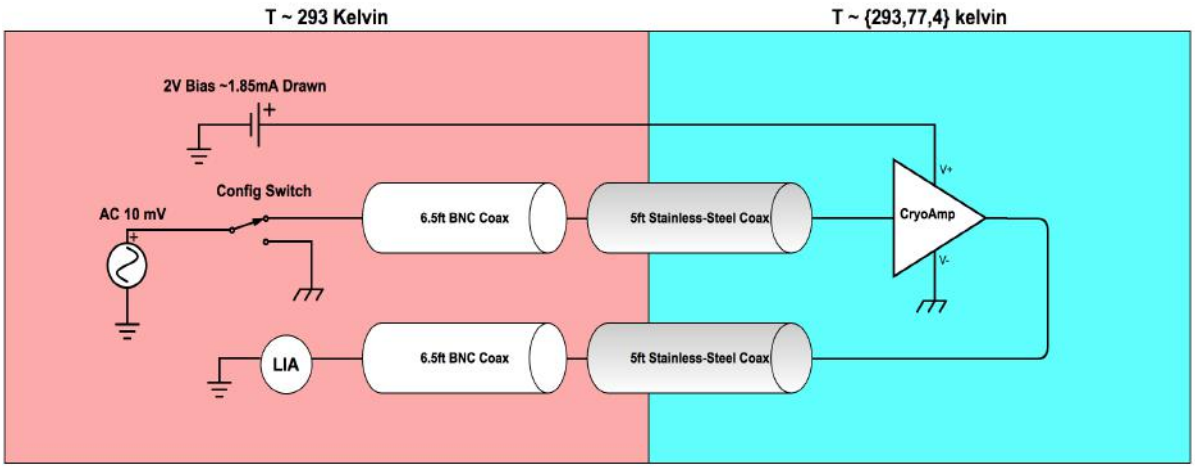

Figure 4.1: Circuit cartoon corresponding to the amplifier transfer function and noise characterization setup. The stainless-steel coaxial cables leading into the dewar have a series resistance of 5.5ohms, while the BNC series resistance is negligible. For 6.5ft of BNC coax and 5ft of stainless coax, we have a parasistic capacitance per coaxial line of about 380pF. The Config Switch represents the configuration difference between measurements of the transfer function and the noise floor of the system.

In Figure 4.1, I present a circuit diagram for the amplifier when it is mounted on this probe in one of two configurations; In one configuration, a 10mV AC excitation is sourced from a Zurich MFLI lock-in amplifier, and is transferred through a coaxial line to the cryogenic amplifier input. After amplification the signal then makes it's way back through an identical coaxial line to an input on the lock-in at room temperature. With the amplifier powered by a 2V bias sourced from a SIM928 module, we sweep the frequency of the excitation in the 0Hz $\rightarrow$ 5MHz range and measure the transfer function of the circuit at various temperatures. In the other configuration we ground the coaxial line that leads to the amplifier input, and measure the noise floor of the circuit with the lock-in using it's built-in spectrum analyzer functionality. In this configuration the noise floor should be dominated by the amplified input noise of the cryogenic amplifier, though we will discuss later where this measurement setup breaks down.

In the transfer function configuration, we hope to capture the bandwidth and gain

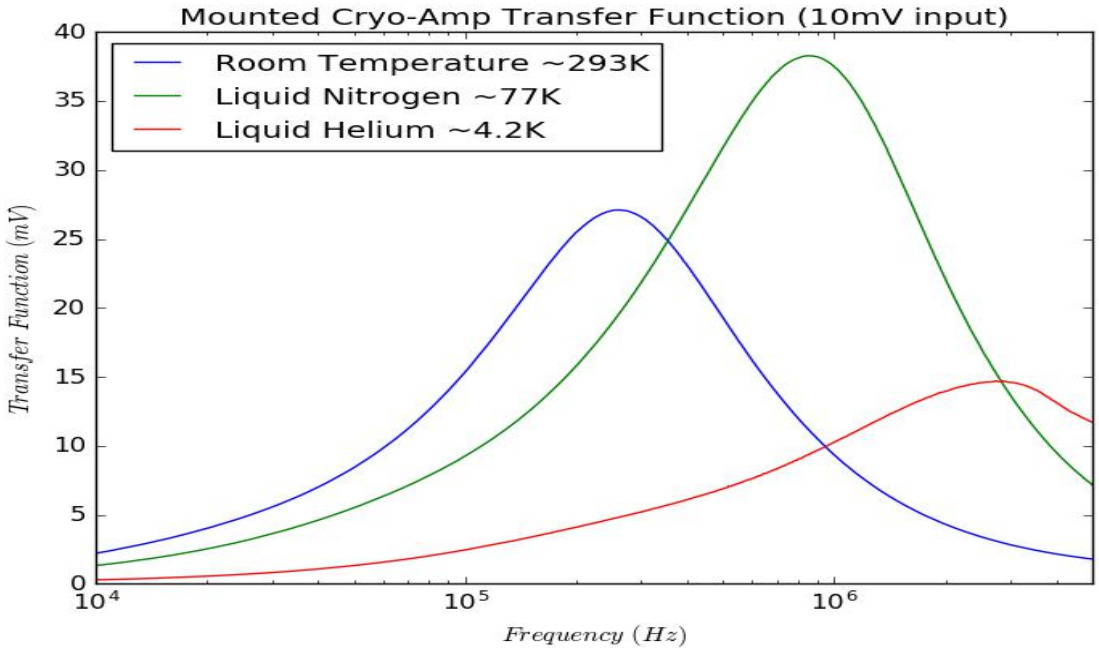

Figure 4.2: First characterizations of the amplifier transfer function for liquid nitrogen and liquid helium temperatures. We note the peak position and heights; for T $\sim$ 300K we have a peak gain of 2.7 positioned at 259kHz, T $\sim$ 77K we have peak gain of 3.8 at 843kHz, T$\sim$4K we have peak gain of 1.4 at 2.77MHz

information of the amplifier. Using the amplifier design described in Figure 3.6 we expect that as temperature decreases the low frequency cutoff of the amplifier should remain mostly unchanged, as this corresponds to passive resistor and capacitor elements in the circuit. Meanwhile we expect the transistor gain to improve with temperature, shifting the high frequency cutoff slightly. The first characterizations of the amplifier transfer function, did not match these expectations.

The old data from this first characterization is shown in Figure 4.2, where we see the peak gain position shifts significantly as a function of temperature, and the gain at helium temperatures is lost, and a bit distorted. In trying to understand why this data did not match up with our expectations, it became apparent that the surface mount capacitors used in the cryogenic amplifier had the X7R thermal coefficient. Capacitors with this thermal coefficient are unstable at low temperatures and their capacitance values can

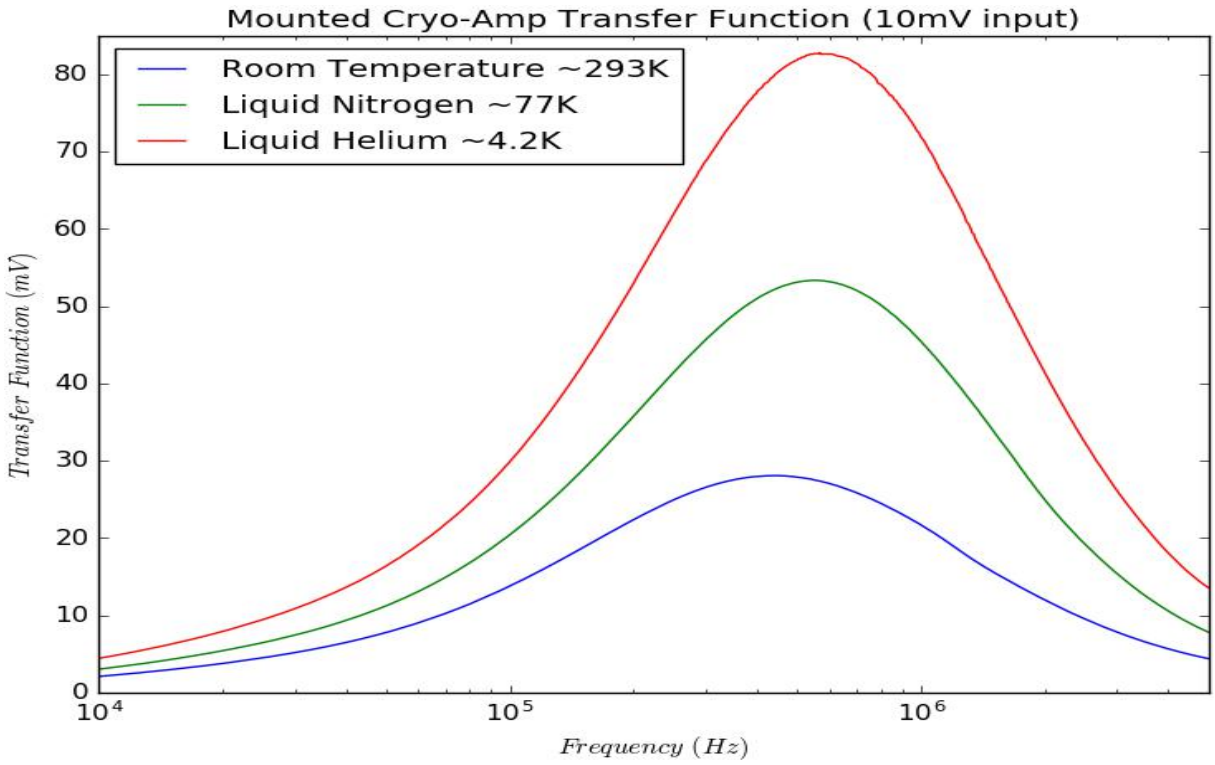

Figure 4.3: Characterizations of the amplifier transfer function for liquid nitrogen and liquid helium temperatures with the correct temperature coefficient. We note the peak position and heights; for T $\sim$ 300K we have a peak gain of 2.8 positioned at 434kHz, T $\sim$ 77K we have peak gain of 5.4 at 572kHz, T$\sim$4K we have peak gain of 8.3 at 575kHz

change substantially. They may also develop a large equivalent series resistance (ESR). This is an easy fix, as there are a number of surface mount components that are known to be robust to cryogenic temperatures. For the next amplifier iteration, we chose resistors with the temperature coefficient TNPW, and capacitors with the temperature coefficient C0G or NPO. The resistance and capacitance values of components with these coefficients change very little as they are taken even to liquid helium temperatures. Figure 4.3 shows the transfer function for the correct values.

In comparing Figures 4.2 and 4.3, I note that there is a 175kHz frequency difference between the room temperature peak positions. This is because at the time of the first characterization, the capacitors C2 and C3 seen in Figure 3.6 were replaced with 4.7nF

capacitors, for lack of 1nF surface mount capacitors. Thus we cannot compare the exact resonance positions and gain values between Figures 4.2 and 4.3, just the frequency shift and gain distortion. With this in mind, we see in Figure 4.3 that after a relatively small frequency shift of 138kHz from room temperature to liquid nitrogen temperature, the peak position shifts only 3kHz when placed into helium. Furthermore, at this final temperature the transfer function is no longer distorted, and there is a peak gain of 8.3 in linear units. The bandwidth of the amplifier at these temperatures is also quite large, with a full width at half maximum of ∼2MHz.

In the second configuration of the probe, used for input noise characterizations, I measured the input noise with the amplifier immersed in liquid nitrogen. In the full Bluefors probe system, if we are planning to optimize the circuit by tuning the resonance position of the bandpass filter to sit at the position of maximum gain in the amplifier, then it is most useful to characterize the noise floor of the amplifier around it's peak gain. In liquid nitrogen, the frequency position of the peak is at 572kHz. I thus set the lock-in demodulation frequency to this value, and measure the noise floor in a small 25kHz bandwidth about this center. Measuring with 10000 averages per data point, I get a value of 7.56 $\frac{nV}{\sqrt{Hz}}$ for the output noise spectral density of this configuration. In the same way I also measure the noise floor of the lock-in amplifier with it's input grounded, and I see a noise spectral density of 2.57 $\frac{nV}{\sqrt{(Hz)}}$. Assuming these noise sources are uncorrelated, then noise spectral densities add in quadrature, so we can deduce an output noise floor for the amplifier;

$$N_{out} = \sqrt{7.56^2 - 2.57^2}\ \frac{nV}{\sqrt{Hz}} \tag{4.1}$$

such that $N_{out} = 7.11\ \frac{nV}{\sqrt{Hz}}$. We get the input noise by simply adjusting for the gain of the amplifier, so $N_{in} = N_{out}/5.4 = 1.3\frac{nV}{\sqrt{Hz}}$. Note however that this noise floor measurement ignores the finite series resistance of the coaxial lines. We are trying to

be sensitive to noise on the order of a few hundreds of $\frac{pV}{\sqrt{Hz}}$, and so the input noise of similar custom cryogenic amplifiers is also on this scale. For instance, the input noise of the amplifier design featured in Figure 3.4 is reported to be $\sim.14\frac{nV}{\sqrt{Hz}}$. Thus the effect of a 5.5 ohm series resistance will become more important at helium temperatures, as the stainless coaxial cables are not fully submerged in liquid, and there is a segment even sitting at room temperature. If even a 1ohm segment of the coaxial cable leading to the amplifier input is sitting at room temperature, then it's Johnson noise spectral density is expected to be $\sim.13\frac{pV}{\sqrt{Hz}}$ which is on the same order as the anticipated input noise of the amplifier, and would upset the measurement. We could ground the input of the amplifier at the liquid helium end and remove the problem of this competing noise source, but then the amplifier transfer function would have a peak at a different frequency, as this is set by the cable capacitance. Thus we would not be able to accurately pin down the demodulation frequency at which we should measure. Furthermore, even if we didn't have a problem of competing noise sources at the input, the gain of this amplifier at liquid helium temperatures is not enough to push a $.14\frac{nV}{\sqrt{Hz}}$ signal above the $\sim2.5\frac{nV}{\sqrt{Hz}}$ noise floor of the lock-in amplifier, without the help of another amplifier like the NF-Corp SA-220F5 pre-amp. For these reasons it is most sensible to hold off measuring input noise around 4 Kelvin until the amplifier can be mounted onto the full Bluefors system, where it's noise floor is more readily disentangled from surrounding sources. However I would conclude from this section that the amplifier is robust, and the transfer function is now behaving as expected. Furthermore, the noise floor that has been measured in liquid nitrogen is promising, and we expect that this component is ready for use in the Bluefors probe system.

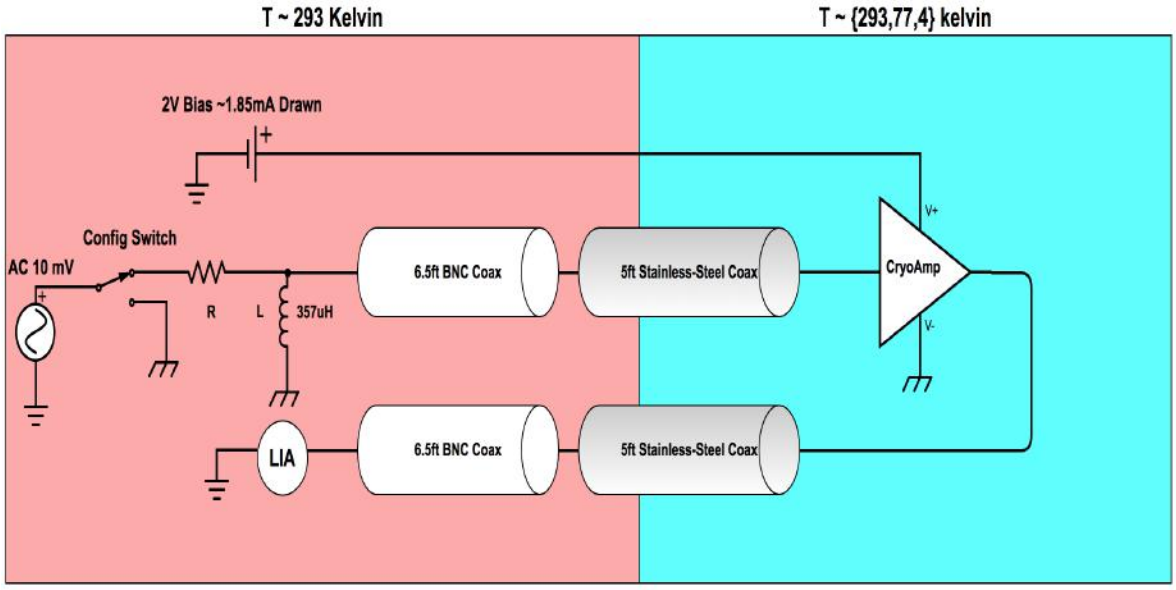

Figure 4.4: Measurement setup used to test the inductor-amplifier system's treatment of a noise signal from a source resistor R, standing in for our graphene sample. The inductor L is a hand wound NbTi solenoid with an equivalent series resistance (ESR) of 19.8 ohms. As usual a SIM928 module supplies the amplifier bias voltage to the amplifier. Each coaxial line has a parasitic capacitance of ∼380pF.

4.2 A Confusing Non-Linear Relationship

Before moving on to the full probe system it is reasonable to check if we can use our hand wound NbTi inductor, along with the custom cryogenic amplifier, to measure the noise spectral density of a resistor at room temperature. The setup for this measurement is as depicted in Figure 4.4, where we see this is only a slight variation of the circuit used for amplifier characterizations.

Here again we have two configurations; in the first we perform an AC sweep with a 10mV excitation going directly from the lock-in to the resistor R, and measure the system's transfer function. In the other configuration, we ground the resistor at the same point where we applied the excitation. In both circuits, our source resistor forms a

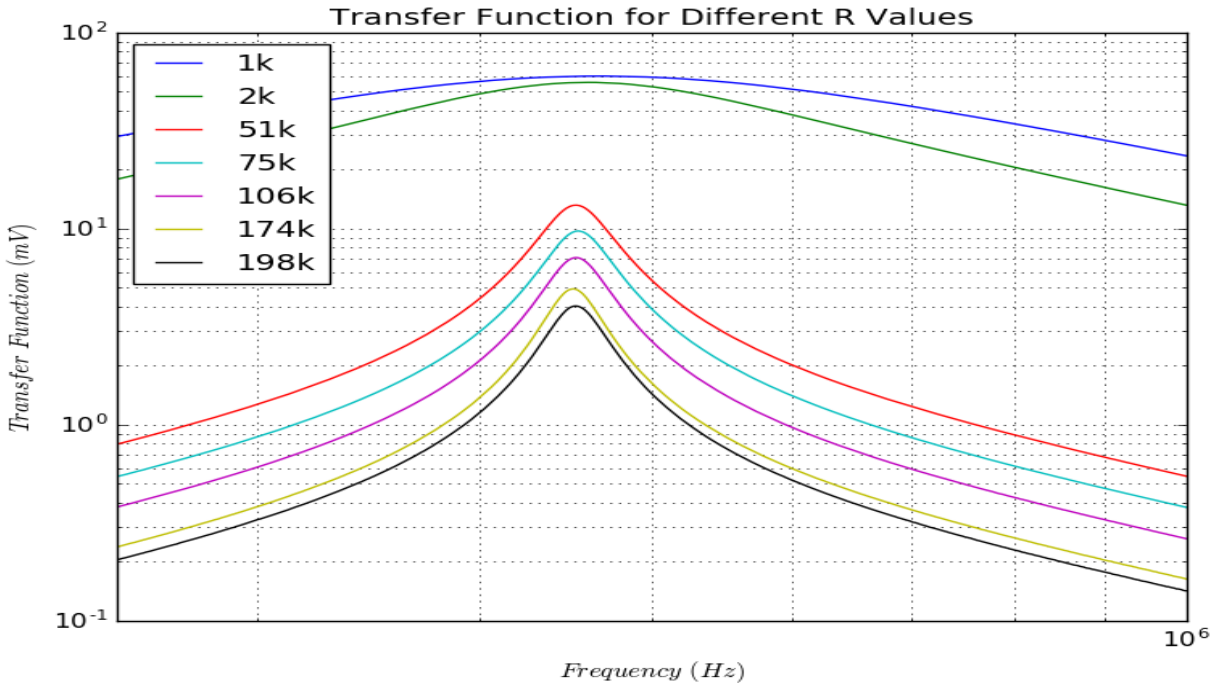

Figure 4.5: Transfer function of the measurement setup with a 10mV input signal and with the amplifier operating at ∼77 Kelvin. While varying the source resistor R, sweeps were taken over the range of 250kHz → 1MHz to capture the behaviour around resonance, which is at 450kHz. We note the transfer function is attenuating for most values of R.

band-pass filter with the parallel inductor and the small cable capacitance (∼380pF) of the coaxial line leading to the amplifier input.

The transfer functions measured for various R values are reported in Figure 4.5, with the amplifier held at liquid nitrogen temperatures. The results seem reasonable; we have an observed resonance of 450kHz, where we would expect a resonant frequency of 432kHz for a 357μH inductor and a 380pF capacitor. This small 18kHz difference is readily explained by the presence of the amplifier, whose gain peak at 572kHz is at a higher frequency than the band-pass resonance. In the combined system, we would thus expect that the peak in the transfer function sits a little above resonance. Furthermore we expect in a typical RLC bandpass filter that increasing R should narrow the bandwidth, or equivalently it should improve the quality factor of the resonator. This expectation is

consistent with the behaviour seen in Figure 4.5. Finally, we expect for an ideal inductor with no parasitic resistance that the transfer function of the band-pass filter should have unity gain at resonance. Thus for an inductor with a finite series resistance, we expect the band-pass to always have sub-unity gain. Circuit simulations in Mathematica and LTSPICE software further predict that in a regime where the inductor has some ESR, the ratio of R to the ESR affects the attenuation at resonance. For an ESR in the inductor of 19.8 ohms at room temperature, we therefore expect that as R increases the peak height at resonance should decrease. Conversely as the value of R decreases the band-pass filter should near unity gain, such that for small R we should be able to see the effect of the amplifier with a linear gain of $\sim$5. This agrees with what is observed in Figure 4.5, where as R increases we see greater attenuation, and for the small 1k and 2k resistance values we see a gain at peak of $\sim$5 as anticipated.

With this understanding of the circuit behaviour, we can move on to noise measurements. I note that the system is not intended to be a primary thermometer, and therefore will not precisely measure absolute temperature. Instead we hope to be sensitive to changes in temperature for constant resistance, or vice versa. By varying R and adjusting for the transfer function, we therefore expect to find a linear relationship between the square of the measured noise and the resistance R. If everything is functioning as desired the slope should be $4k_BT$ from to the Johnson-Nyquist formula, with maybe a noise offset that is the result of the background of our system.

Figure 4.6 shows the noise data for different R values, where we have adjusted for the gain of the transfer function corresponding to each R. Also plotted is the linear slope we would expect from the Johnson noise of resistors at a constant temperature T = 293 Kelvin. The non-linearity of this measured noise with respect to R, and the disparity with the Johnson Nyquist behaviour we anticipate, has been a major source of confusion. After some thought, we have established a few possible explanations; For one,

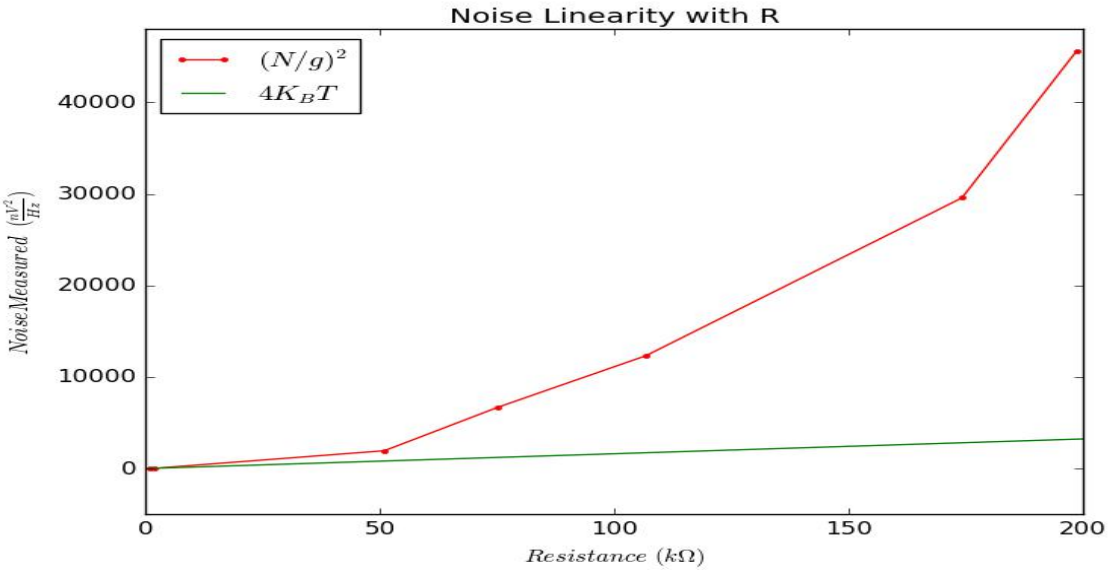

Figure 4.6: The noise spectral density of the resistor R is measured by taking the noise spectral density N seen at the lock-in and adjusted for the transfer function g. The square of this value is then plotted in red as a function of R. In green, the expected Johnson noise slope for resistors at T=293 Kelvin is shown with no offset.

it is possible that the large reactance of the inductor is pushing the cryogenic amplifier into a region of instability, whereupon a ring oscillator is formed that creates a fictitious signal around the expected resonance point. This possibility seems unlikely, as with the capacitors C2 and C3 of the amplifier design in Figure 3.6 the amplifier should be stable in the frequency range where it is used. Furthermore, it is not clear why the noise contribution from the ring oscillator effect would vary with the source resistor R. Nonetheless, we could test for this amplifier instability by varying C2 and C3. A more likely hypothesis is that the noise from the ESR of the inductor is actually dominating the observed voltage signal. To see how this is possible, Figure 4.6 gives a more precise view of the band-pass filter.

While signal from the source S1 is attenuated through a band pass filter formed with R as we expect, the source S2 sees a band pass filter with the same resonance point, but no attenuation. In fact, circuit simulations in LTSPICE show the signal from source S2

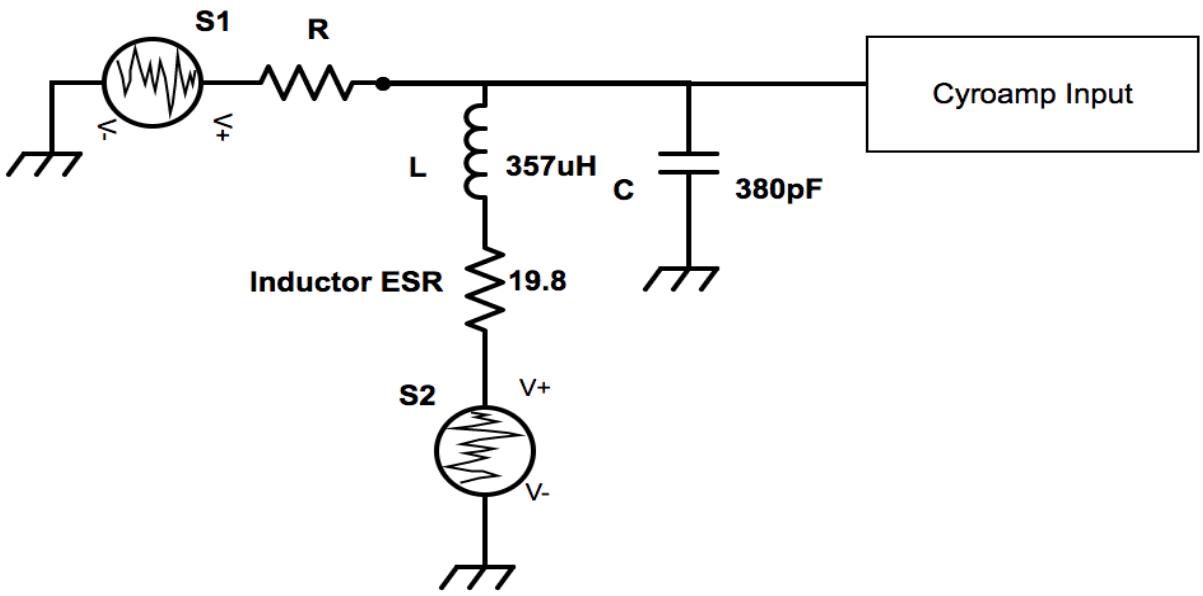

Figure 4.7: Circuit model of the bandpass filter sitting in front of the cryogenic amplifier input. The resistors in the circuit are modeled as a noise source in front of an ideal noiseless resistor. As such the two sources S1 and S2 contribute to the noise signal that is seen at the input, and each source sees a different transfer function.

actually undergoes a significant voltage amplification before it reaches the amplifier input (See Figure 4.8). From these simulations it is predicted that as the resistor R increases, two things happen; First, the portion of the signal S1 seen at the amplifier will decrease with R, as we have already seen. Second, the signal S2 undergoes voltage amplification at constant power, reducing the associated current before it reaches the input. Some signal is lost across R, but the effect will be greatest when R is small compared to the input impedance of the amplifier. Thus as R increases, the portion of S2 seen at the amplifier input will increase. The combination of these two effects would mean S2 increasingly dominates S1 in the observed voltage spectral densisty.

If this effect is the cause of the problem then it should also be straightforward to fix. If we repeat these tests with both the amplifier and inductor immersed in liquid helium, then the NbTi inductor should be superconducting, removing it's ESR and the source S2 altogether. In addition, as the voltage amplification of S2 is carrier out by passive

Figure 4.8: Simulation of the transfer functions experienced by signals S1 and S2 of Figure 4.7 as they propagate to the input of the cryogenic amplifier. The simulation sources a 10mV excitation in the place of S1 and S2 for comparison, and in this case the resistor R is taken to be 10k. In green, the noise signal S1 of the resistor R is seen to be attenuated by a factor of $\sim$.8 at resonance. Meanwhile in red, the signal S2 is amplified by a factor of 8.5 at resonance. The transfer functions for both signals share a resonance point at $\sim$ 432kHz.

components with no net gain in power, then by taking the power spectral density of the signal, source S2 should not be as outstanding. However due to a lack of liquid helium, these tests will not have been performed in time for the writing of this paper.

Section 5

Conclusion

The goal of this project was to develop a secondary thermometry system that makes use of the precisely defined resistance of the FQHE in a graphene heterostructure to track electron temperatures. At this point in time, we have settled on the design for the probe, as described in Section 3. All of the components of this design have either been bought or built, and the assembly is nearing completion. For this design a custom cryogenic RF-amplifier was constructed and characterized in Section 4.1, and it is now ready for use. The only major obstacle standing in the way of using this system, and making a temperature measurement of a FQH sample, is the non-linear behaviour described in Section 4.2. We will be able to move on from this delay as soon as our system can report that the measured noise spectra has a linear relationship with the source resistance, corresponding to a slope of $4k_BT$. Until that time this thesis stands predominantly as a guide to help new members of the lab become familiar with the project and what we hope to accomplish. It also stands as a reference that should facilitate the completion of the project for those who will inherit it.

Bibliography

[1] I. Ivanov, M. Bonn, Z. Mics, and D. Turchinovich, *Perspective on terahertz spectroscopy of graphene*, *EPL (Europhysics Letters)* **111** (sep, 2015) 67001.

[2] A. A. Zibrov, C. Kometter, H. Zhou, E. M. Spanton, T. Taniguchi, K. Watanabe, M. P. Zaletel, and A. F. Young, *Tunable interacting composite fermion phases in a half-filled bilayer-graphene Landau level*, *Nature* **549** (sep, 2017) 360.

[3] A. Y. Kitaev, *Fault-tolerant quantum computation by anyons*, 9707021v1.

[4] G. Moore and N. Read, *Nonabelions in the fractional quantum hall effect*, .

[5] N. R. Cooper and A. Stern, *Observable bulk signatures of non-abelian quantum hall states*, *Phys. Rev. Lett.* **102** (Apr, 2009) 176807.

[6] E. Majorana, *Teoria simmetrica dell'elettrone e del positrone*, *Il Nuovo Cimento (1924-1942)* **14** (Sep, 2008) 171.

[7] A. Sivaguru, *Majorana Fermions*. Qfff msc dissertation, Imperial College London, 2012.

[8] M. Dolev, M. Heiblum, V. Umansky, A. Stern, and D. Mahalu, *Towards identification of a non-abelian state: observation of a quarter of electron charge at ν =5/2 quantum Hall state.*, *Nature* **452** (2008) [0802.0930].

[9] D. Abbott, B. R. Davis, N. J. Phillips, and K. Eshraghian, *Simple Derivation of the Thermal Noise Formula Using Window-Limited Fourier Transforms and Other Conundrums*, .

[10] C. Nayak, S. H. Simon, A. Stern, and M. Freedman, *Non-Abelian anyons and topological quantum computation*, .

[11] G. Batey and G. Teleberg, *Principles of Dilution Refridgeration - A brief technology guide*, 2015.

[12] Z. Iftikhar, A. Anthore, S. Jezouin, F. Parmentier, Y. Jin, A. Cavanna, A. Ouerghi, U. Gennser, and F. Pierre, *Primary thermometry triad at 6 mK in mesoscopic circuits*, 1610.0371.

[13] U. Tietze, C. Schenk, and G. Eberhard, *Electronic Circuits Handbook for Design and Applications*. Springer, 2 ed., 2002.